## POLITECNICO DI TORINO
## Repository ISTITUZIONALE

Magnetic, Thermal and Structural Scaling of Synchronous Machines

(Article begins on next page)

22 September 2024

# Magnetic, Thermal and Structural Scaling of Synchronous Machines

Gaetano Dilevrano
*Dipartimento Energia Galileo Ferraris*
*Politecnico di Torino*
Turin, Italy
gaetano.dilevrano@polito.it

Paolo Ragazzo
*Dipartimento Energia Galileo Ferraris*
*Politecnico di Torino*
Turin, Italy
paolo.ragazzo@polito.it

Simone Ferrari
*Dipartimento Energia Galileo Ferraris*
*Politecnico di Torino*
Turin, Italy
simone.ferrari@polito.it

Gianmario Pellegrino
*Dipartimento Energia Galileo Ferraris*
*Politecnico di Torino*
Turin, Italy
gianmario.pellegrino@polito.it

Timothy Burress
*Energy Science and Technology Directorate*
*Oak Ridge National Laboratory*
Knoxville, USA
burressta@ornl.gov

*Abstract*—A fast and accurate method for scaling the dimensions and the performance of Permanent Magnet Synchronous Machines (PMSMs) is proposed, based on the use of flux linkage maps. Starting from a reference design, the scaled machine is designed to comply new peak torque and power, maximum operating speed, voltage and current specifications in seamless computational time. A new design plane is introduced, permitting the minimization of the stack length of the scaled design. The analysis covers the scaling of losses and the rules for scaling the water-glycol stator cooling jacket, which is a common cooling setup for PMSMs in traction application. The torque versus speed characteristics, the efficiency map and the thermal limit of the scaled design are obtained in seamless computational time without need of dedicated finite-element simulations. The e-motor of the BMW i3 is the reference design and the moto-generator 2 of the 4-th generation Toyota Prius is the target application for showcasing the proposed method.

*Index Terms*—AC motors, Electric motors, Permanent magnet machines, Traction motors, Algorithm design and analysis.

## I. INTRODUCTION AND MOTIVATION

Permanent Magnet (PM) synchronous machines (PMSMs) are the state of the art solution for vehicular traction [1], and a competitive option in many fields of application, as aviation [2], wind power generation [3] and railway traction [4]. Among the most urging challenges [5], the high and volatile cost of PM materials [6] pushed the industry towards the minimization of the PM quantity by exploiting the reluctance torque component [1]. Also, research efforts are dedicated to the use of non-rare-earth magnet solutions, as ferrite on synchronous reluctance (SyR) [7] machines. Nevertheless, rare-earth magnet based PMSMs remain the best-in-class solution for traction.

Several design approaches to design PMSMs are found in literature. Many are based on optimization algorithms involving significant computational time [8]. The Design of Experiments (DoE) helps minimizing the computational time of the optimization process preserving the accuracy and the reliability [9] by intelligent sampling of the simulated machines

in the variables space. Purely analytical design equations [10] can be employed, but they are known for poor accuracy. Whatever the adopted design method, the starting point of a new PMSM design is very often an existing design with different dimensions and output specifications. The use of scaling laws is an established engineering practice; the similitude laws allow to evaluate a new machine of larger or smaller dimension in seamless computational time. Reference [11] addresses the magnetic scaling of PMSMs, including variation of the stack outer diameter, active length and number of turns. The analysis was extended in [12] to the scaling of the efficiency maps.

This paper improves the use of existing magnetic scaling laws for the accurate and optimized design of a new PMSM with given dimensional constraints (stack diameter and length) and power converter constraints (phase current and DC voltage limits). Besides evaluating the performance and efficiency map of the scaled designs in seamless time, the method permits to minimize the volume of the new machine. The structural and thermal aspects of the scaled design are also covered in the paper. In [13], the thermal model is scaled under the oversimplifying assumption of a constant heat exchange coefficient between the stack and the coolant. This is improved
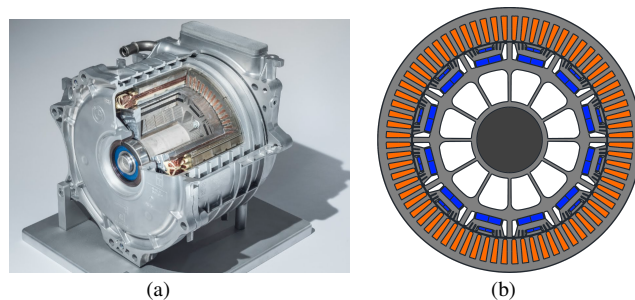


Fig. 1. BMW i3 Traction Electric Motor Type EMP242 of 2016. a) Machine cut-off; b) Cross section of the active parts.

TABLE I
BMW I3 AND PRIUS GEN IV MG2 MOTOR RATINGS [14]

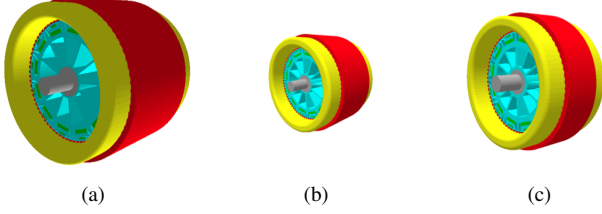|  |  | i3 | Prius MG2 |  |
|---|---|---|---|---|
| Max current | $I_{max}$ | 530 | 226 | [Apk] |
| Max torque | $T_{max}$ | 250 | 163 | [Nm] |
| DC link voltage | $V_{dc}$ | 355 | 600 | [V] |
| Nominal speed | $n_{base}$ | 4500 | 3500 | [rpm] |
| Max speed | $n_{max}$ | 11400 | 17000 | [rpm] |
| Max power | $P_{max}$ | 125 | 53 | [kW] |
| Pole pairs | $p$ | 6 | 4 |  |
| Outer diameter | $D$ | 242 | 215 | [mm] |
| Stack length | $L$ | 132 | 60 | [mm] |
| Volume | $V$ | 6.1 | 2.2 | [L] |
| Turns | $N_s$ | 18 |  |  |



Fig. 2. a) BMW i3 reference; b) Scaled Mot1; c) Scaled Mot2.

here, where the guidelines for scaling the cooling jacket are given and the thermal limit of the resulting machine is analytically evaluated.

The e-motor of the BMW i3 (cross section in Fig.1) is the reference design of this study, scaled to match the specifications of the moto-generator 2 (MG2) of the Toyota Prius Gen IV in two variants: one respecting the outer diameter and aspect ratio of the target Prius machine (Mot2) and one with a smaller diameter as suggested by the stress limit at maximum operating speed (Mot1), see Fig. 2 The ratings of the considered machines are reported in Tab.I [14]. The proposed method is integrated in the open-source design and simulation platform SyR-e [15].

## II. PROPOSED SCALING METHOD

The following scaling factors are defined:

$$k_D = \frac{D}{D_0} \qquad k_L = \frac{L}{L_0} \qquad k_N = \frac{N_s}{N_{s0}} \quad (1)$$

They represent respectively the ratio of the outer stator diameter $D$, stack length $L$ and number of turns in series $N_s$ to the respective quantities of the reference machine,
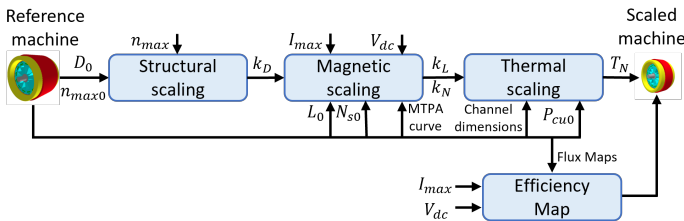


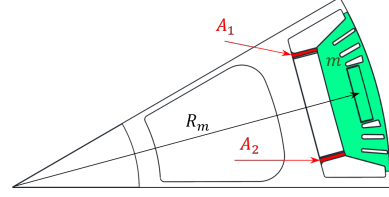Fig. 3. Flowchart of the proposed scaling process.



Fig. 4. Structural behavior on a PMSM rotor with hanging mass and ribs highlighted.

indicated with 0. Length scaling and rewinding are well known procedures determined by intuitive linear relationships. Radial scaling considers that all the dimensions of the cross section are scaled according to the stator outer diameter ratio $k_D$, and that the flux density field distribution is maintained when the current density is scaled with the diameter [11]. The flowchart of the proposed method is represented in Fig.3.

### A. Structural scaling

Structural scaling is considered first, for its direct impact on the diameter ratio, given the maximum operating speed. Considering the rotor in Fig.4 rotating at maximum speed $n_{max}$, the force generated by the hanging mass $m$ placed at radial position $R_m$ is sustained by the highlighted ribs with total cross section equal to $(A_1 + A_2)$. The resulting stress is equal to:

$$\sigma_{max} = \frac{F}{A_1 + A_2} = \frac{(\frac{\pi}{30})^2 \cdot m \cdot R_m \cdot n_{max}^2}{A_1 + A_2} \propto D^2 n_{max}^2 \quad (2)$$

The stress scaling rule at maximum speed is then:

$$\frac{\sigma_{max}}{\sigma_{max0}} = \frac{D^2 \cdot n_{max}^2}{D_0^2 \cdot n_{max0}^2} \quad (3)$$

which tells that, at imposed stress conditions, the diameter ratio follows the inverse of the speed ratio. Assuming that the stress limit does not change after scaling, the needed diameter ratio is determined after the ration of maximum operational speeds:

$$k_D = \frac{n_{max0}}{n_{max}} \quad (4)$$

To mechanically evaluate the reconstructed model of the benchmark, structural analysis are performed by means of an in-built SyR-e tool. It is based on Matlab Partial Differential
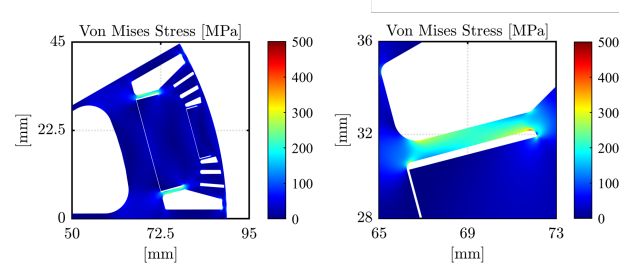


Fig. 5. Mechanical FEA results on BMW i3 at 11400 rpm.

Equation (PDE) Toolbox that allows to solve differential equation using FEA. The custom geometry is imported from the FEMM file and in each region the mechanical proprieties are set according to the material, i.e. iron, air or magnet and the boundaries are fixed. Then the centrifugal load is applied at the selected input speed. Furthermore, the mesh size can be manually varied, however as default it is set at one order of magnitude lower than the drawing tolerance. The output of the simulation is the stress results in Fig. 5. The structural analysis performed at the maximum speed of 11400 rpm ensures the rotor integrity.

*B. Scaling of flux maps*

Reference is made to the known magnetic scaling laws of [11], this time applied to the flux and loss maps of the reference machine as a whole and not the single (e.g. nominal) operating point.

Fig. 6 shows the flux maps of the reference machine, obtained by multi-step FEA simulations on a regular current grid in the $dq$ plane. For the sake of a fast evaluation, transient FEA are substituted by magneto-static 2D FEA with sequenced rotor positions. In addition, geometric and electric symmetry is exploited and parallel computing is adopted to further speed-up the evaluation. The $dq$ flux linkage average, torque average and peak-to-peak torque values from the same simulated points are saved in matrices. To evaluate the reference machine, a current grid of 15x15 points were used, each with 15 rotor positions on 60 electrical degrees, evaluated in less than 15 minutes using a workstation with Intel Xeon E5-2690 v4 CPU, 14 cores and 32GB RAM.

The $d$ and $q$ flux maps vary as:

$$\frac{\lambda_d(i_d, i_q)}{\lambda_{d0}(i_{d0}, i_{q0})} = k_N k_L k_D \qquad \frac{\lambda_q(i_d, i_q)}{\lambda_{q0}(i_{d0}, i_{q0})} = k_N k_L k_D \quad (5)$$

under the assumption that the current components are remapped to preserve the magnetic flux density distribution, i.e. with the current density varied according to the diameter [11]:

$$\frac{i_d}{i_{d0}} = k_D k_N^{-1} \qquad \frac{i_q}{i_{q0}} = k_D k_N^{-1} \qquad (6)$$

The end-winding flux linkage terms are neglected in (5) for simplicity, but they can be accounted for using the scaling law
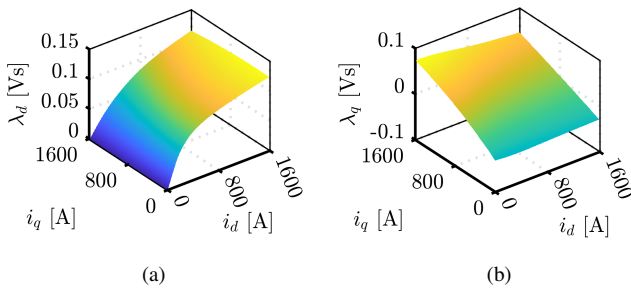


(a)                                (b)

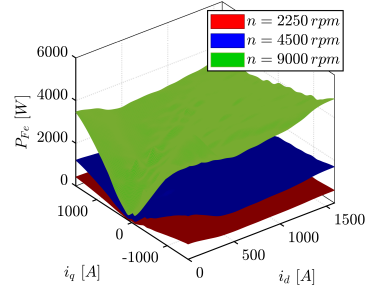Fig. 6. Flux maps of the reference machine: (a) $d$-axis flux linkage and (b) $q$-axis flux linkage.



Fig. 7. Iron loss map of the reference machine function of the rotor speed.

valid for inductances [11].

The electromagnetic torque map (product of flux linkage and current) is therefore scaled and remapped as:

$$\frac{T(i_d, i_q)}{T_0(i_{d0}, i_{q0})} = k_D^2 k_L \qquad (7)$$

Note that the domain of representation of the flux maps of the reference machine must be large enough to cover the maximum Ampere-turns condition of the target machine.

*C. Scaling of losses*

The iron and PM losses of the reference machine are mapped over the $dq$ current domain at a single value of speed. Speed variation is accounted using the Steinmetz loss model of the electrical steel, and quadratic variation with speed for the PM loss term [16].

The iron loss map of the reference motor is reported in Fig. 7. The FEA simulation of each $(i_d, i_q)$ point covers a rotor excursion of 180° and uses the symmetry properties of the alternated waveforms to retrieve information on the whole electrical period. Iron loss computation contemplates both major and minor hysteresis loops as well as the DC bias effect in the case of the rotor. The loss maps are retrieved with a current grid of 15x15 points, each with 180 rotor positions on 180 electrical degrees, evaluated in around 90 minutes using the reference workstation. The details on the flux and iron loss maps can be found in [16].

Considered that the $(i_d, i_q)$ domain is scaled for flux density conservation, the iron loss map are scaled with the volume of the stack, that is according to $D^2 L$, and the same law holds for PM loss.

$$\frac{P_{Fe}(i_d, i_q)}{P_{Fe0}(i_{d0}, i_{q0})} = k_D^2 k_L \qquad (8)$$

The stator resistance is scaled as:

$$\frac{R_s}{R_{s0}} = \frac{k_N^2}{k_D^2} \cdot \left( k_L \cdot \frac{L_0}{L_0 + l_{ew0}} + k_D \cdot \frac{l_{ew0}}{L_0 + l_{ew0}} \right) \qquad (9)$$

where $l_{ew0}$ is the end-winding length of the reference machine, which is assumed to scale proportionally with the diameter. Therefore, the DC copper loss is computed as $P_{Cu} = \frac{3}{2} R_s |i_{dq}|^2$ for both the reference and scaled machines.

Note that the AC copper loss is neglected as they will be object of future works.

### D. New $(L, N_s)$ design plane at MTPA conditions

Once the diameter scaling ratio $k_D$ is determined, for example according to the maximum speed constraint (4), the selection of $k_L$ and $k_N$ is not unique and it is addressed using the novel length-turns plane displayed in Fig.8. The plane refers to MTPA conditions and displays the peak torque at maximum inverter current and the base speed at maximum inverter voltage of the scaled design, function of the scaled length and number of turns.

The construction of the length-turns plane starts from the normalized MTPA law of the reference machine, consisting of the $dq$ current and flux linkage components function of torque, retrieved numerically by manipulation of the flux linkage maps. The MTPA curves of the reference machine are normalized following the respective scaling quantities, as visible in Fig. 9. The figure shows how the maximum current condition of the reference machine defines the peak torque value, and how such peak torque further defines the base flux linkage value. Finally, the base flux linkage determines the base speed according to the inverter voltage limit equation (10).

$$\left\| R_s \cdot (i_{dq})_{max} + j \cdot n_{base} \cdot \frac{\pi p}{30} \cdot (\lambda_{dq})_{base} \right\| = \frac{V_{dc}^2}{3} \quad (10)$$

where $j$ is the complex operator used for space vector representation and $p$ is the number of pole pairs. The voltage limit condition (10) defines the base speed for both the reference and scaled designs, with reference to the respective dc-link voltage values.

Given the reference MTPA law, the design plane is built as follows. The maximum current and dc-link voltage of the target machine are considered. The diameter of the scaled machine is also preliminarily determined, as said. Considering a pair of arbitrary values of length and number of turns, the normalized peak torque is evaluated after the normalized maximum current. Then, the normalized base flux linkage is determined after the peak torque, and the base speed is
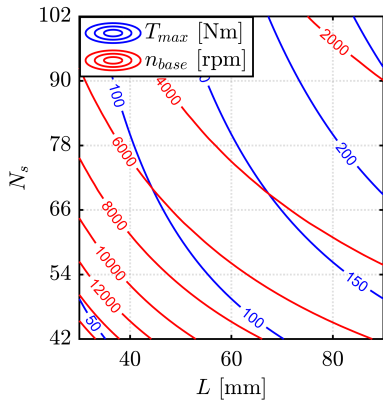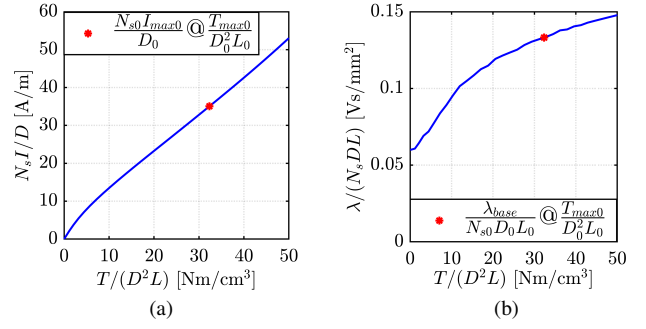


Fig. 9. Normalized MTPA curves of the reference machine function of normalized torque.

retrieved according to (10). The process is repeated for the range of considered values of length and turns to build the plane. It must be remarked that the current and voltage limits of the target machine refer to the target application with no constraint by the reference design, i.e. they do not rigidly follow the scaling of dimensions, torque and speed. This is another key contribution of the paper.

### E. Scaling of the cooling jacket dimensions

The heat transfer equations are extracted from [17] and the channel cross dimensions are defined in Fig.10-a. The spiral water jacket is scaled imposing **constant flow rate** $Q$ **and constant Reynolds number** $Re$, and varying the dimensions of the channel cross section accordingly. Constant $Re$ guarantees that the turbulent flow condition is maintained after scaling, whereas the flow rate values in use in automotive are quite independent of the size of the e-motor. The hydraulic diameter $D_h$ is defined (11) for a tube of rectangular section.

$$D_h = \frac{2 \cdot w_c h_c}{w_c + h_c} \quad (11)$$

The Reynolds number (12) is defined accordingly. Note that $\rho$ is the mass density and $\mu$ is the dynamic viscosity of the fluid, which is a 50%-50% mixture of water and glycol.

$$Re = \rho \frac{Q}{w_c \cdot h_c} \frac{D_h}{\mu} \propto \frac{Q}{w_c + h_c} \quad (12)$$

The type of flow (laminar or turbulent) depends on $Re$. The threshold values are reported in Tab. II for the considered fluid.

Equation (12) suggests that for fixed $Re$ and $Q$ the sum of the channel height and width must be kept constant when changing the motor's dimensions. This **constant perimeter** channel scaling law is translated into the proposed rule (13).

$$w_c + h_c = const \rightarrow \begin{cases} \frac{h_c}{h_{c0}} = k_D \\ \frac{w_c}{w_{c0}} = 1 + \frac{h_{c0}}{w_{c0}} \cdot (1 - k_D) \end{cases} \quad (13)$$

Where it is decided that the channel height follows the diameter ratio $k_D$ and the channel width is adapted accordingly (see Fig. 11). Other choices are possible.



Fig. 8. $(L, N_s)$ design plane obtained with $k_D = 0.67$ for the i3 motor.

## F. Scaling of the heat exchange coefficient

The coolant thermal conductivity is function of the Prandtl and Nusselts numbers. The first is defined as:

$$P_r = \frac{\mu \cdot c_p}{k} \tag{14}$$

where $c_p$ [J/kg/°C] is the specific heat of the fluid and $k$ [W/m/°C] is the thermal conductivity.

The Nusselt number for the turbulent flow is defined as (15). Note that constant $Re$ corresponds to constant $Nu$ for a defined fluid.

$$Nu = \frac{f/8(R_e - 1000)P_r}{(1 + 12.7(f/8)^{0.5}(P_r^{2/3} - 1))} \tag{15}$$

Fixed the geometric law (13), the coolant thermal conductivity $h$ [W/°C/m$^2$] varies according to (16), i.e. independently of axial length and in inverse proportion of the channel cross-sectional area:

$$h = \frac{Nu \cdot k}{D_h} \propto \frac{1}{D_h} \propto \frac{1}{w_c \cdot h_c} \tag{16}$$

The scaling law is obtained:

$$\frac{h}{h_0} = \frac{w_{c0}}{k_D \cdot (w_{c0} + h_{c0} \cdot (1 - k_D))} \tag{17}$$

telling that a machine of smaller diameter will benefit from better heat extraction and vice-versa, as also visible in Fig.11. This also tells that when scaling up the diameters, some relaxation of the proposed assumptions might be considered (e.g. increasing the fluid flow rate).

## G. Stall torque of the scaled machine

The steady-state torque at stall conditions $T_N$ is predicted using the simplified thermal network in Fig.10-b, under the assumption of constant temperature rise at steady state after scaling. The thermal resistance between iron and water jacket $R_{Fe,WJ}$ is expressed analytically (18).

### TABLE II
### REYNOLDS NUMBER AND FLUID FLOW TYPE CORRELATION

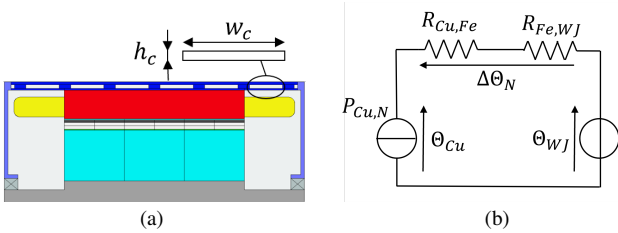| Reynolds Number | Fluid flow type |
|---|---|
| $Re>4000$ | Turbulent |
| $2300<Re<4000$ | Transition |
| $Re<2300$ | Laminar |



Fig. 10. a) Channel dimensions nomenclature; b) Simplified thermal network at stall conditions.
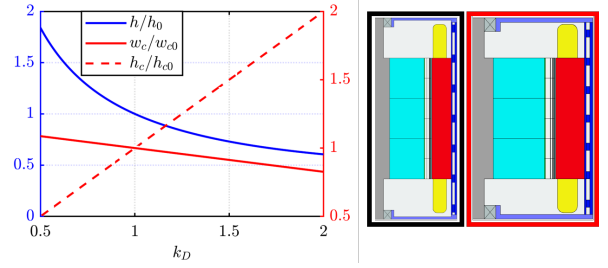


Fig. 11. Thermal conductivity vs $k_D$ following the law (13) and effect of radial scaling on the cooling jacket: $k_D = 1$ is red boxed and $k_D = 0.67$ is black boxed.

$$R_{Fe,WJ} = \frac{1}{h \cdot A} \tag{18}$$

And it can be scaled according to:

$$\frac{R_{Fe,WJ}}{R_{Fe,WJ0}} = \frac{w_{c0} + h_{c0} \cdot (1 - k_D)}{k_L \cdot k_D \cdot w_{c0}} \tag{19}$$

Provided that the steady-state temperature rise of the reference machine $\Delta\Theta_{N0}$ and related DC copper loss $P_{Cu,N}$ are known from simulation or experimental data, the the thermal resistance between copper and iron of the initial machine is calculated using the network of Fig.10-b.

$$R_{Cu,Fe0} = \frac{\Delta\Theta_{N0}}{P_{Cu,N0}} - R_{Fe,WJ0} \tag{20}$$

where $\Delta\Theta_{N0}$ is the difference between the average copper temperature and the average coolant temperature. The scaling rule for the copper to iron thermal resistance (21) is found under the assumption of the heat flow cross section scaling with $D$ and $L$ and the heat flow length scaling with $D$:

$$\frac{R_{Cu,Fe}}{R_{Cu,Fe0}} = \frac{1}{k_L} \tag{21}$$

Imposing that the average copper to coolant temperature rise is constant, the sustainable copper loss at stall are calculated for the scaled machine.

$$\frac{P_{Cu,N}}{P_{Cu,N0}} = \frac{R_{Cu,Fe0} + R_{Fe,WJ0}}{R_{Cu,Fe} + R_{Fe,WJ}} \tag{22}$$

Given the electrical resistance of the scaled machine (9), the continuous current at stall can be evaluated and the respective torque is extrapolated from the scaled MTPA curves.

## III. EFFICIENCY MAP AND THERMAL SIMULATIONS

The efficiency map of the reference machine is evaluated using the flux and loss maps as in [16]. The same procedure is used for the scaled machines using the scaled flux and loss maps, with no extra FEA simulation. Once the flux and loss maps are scaled, the optimal working point for each speed and torque combination is found taking into account the MTPA and MTPV (Maximum Torque per Voltage) laws and the current and voltage limits. Fig.12 reports the efficiency map of the reference machine. Note that the map refers to
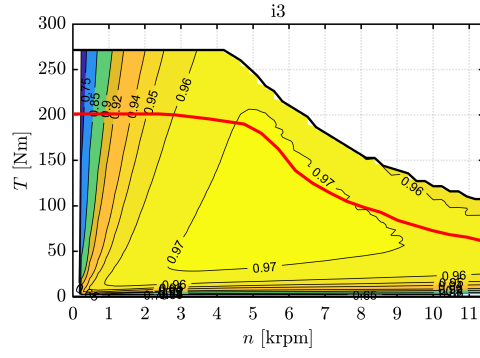
Fig. 12. Efficiency map and continuous torque curve (red) of the BMW i3. Winding temperature 180°C, PM temperature 150°C.
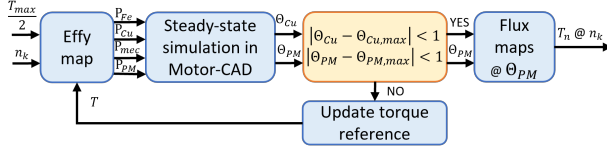


Fig. 13. Flowchart of the continuous performance evaluation for the speed value $n_k$ [rpm].

fixed PM and copper temperature values. The steady-state torque limit is calculated with iterative static simulations in Ansys Motor-CAD. First, the model is created in Motor-CAD with the automatized process presented in [18] for SyR machine, now extended to PMSMs. Then, Motor-CAD is exploited to compute the continuous torque function speed, with the custom process reported in Fig. 13. This is repeated for each speed value and takes 10 minutes overall with the reference working station, if 20 speed steps are evaluated. Given all the loss contributions in each point of the efficiency map, a SyR-e script iterates the losses from these maps in the Motor-CAD Thermal module until one of the two target temperatures (copper 180°C and magnet 150°C) are reached. When one of the two target temperatures is reached, the script checks if the other temperature is below the limit; if not, the iterations are resumed until this condition is fulfilled. For each continuous operating point, the obtained magnet



Fig. 14. Interpolation of flux curves at an arbitrary PM temperature of $65°C$ and relative error. Curves at $\Theta_{PM} = 20°C$ and $\Theta_{PM} = 150°C$ are FEA computed. The dashed lines refer to the cross-saturation effect.

temperature is used to update the flux maps and retrieve the continuous torque. The flux map at a given magnet temperature is retrieved by linear interpolation between two flux maps FEA computed at the PM upper and lower temperature limits of 20°C and 150°C. An example is provided in Fig. 14, where the flux curves interpolated at 65°C show insignificant error with reference to the results of dedicated FEA simulations. Thus, the new operating point corresponding to the feasible loss is re-calculated and the continuous torque value saved. Note that the PM temperature effect on the loss is neglected. Applying the described method, the continuous performance for the reference machine are obtained and displayed in Fig. 18.

## IV. CASE STUDIES

The described scaling procedure are applied to the target specifications of the Toyota Prius IV MG2, reported in Tab. I. Two directions are investigated in the following:

A) **fixed maximum speed**: the scaled motor has to structurally sustain the target maximum speed with freedom on the stack diameter;

B) **PRIUS dimensions**: the scaled motor has to match the target dimensions, stack diameter and length, with freedom on the sustainable maximum speed.

The scaled motors are summarized in terms of magnetic and thermal performance respectively in Tab. III-IV.

### A. Design case 1: diameter set by the maximum speed

The diameter ratio is fixed according to the maximum speed values (4):

$$k_D = \frac{n_{max0}}{n_{max}} = \frac{11400}{17000} = 0.67 \qquad (23)$$

The resulting stack diameter of 162 mm, dictated by the maximum speed constraint, is significantly smaller than the one of the Toyota MG2.

With the diameter fixed, the other scaling factors $k_L$ and $k_N$ must be determined to fulfill the peak torque and base speed specifications (163 Nm and 3500 rpm), given the inverter constraints of the Prius IV MG2 ($I_{max} = 226$ Apk and $V_{dc} = 600$ V). The length-turns scaling plane in Fig. 15 is used to highlight feasible and optimal solutions.

The estimated stall torque contours are also reported. The domain where both specifications are fulfilled is highlighted in green. A reasonable criterion to select the best design is to minimize its volume, i.e. its stack length. This leads to individuate the Mot1 at the left corner of the green area and having the feasible number of turns of 72. The minimum-length design Mot1 has the coordinates $k_L = 0.536$ ($L = 71$mm) and $k_N = 4$ ($N_s = 72$).

The continuous stall torque of Mot1 is predicted to 50Nm by the analytical thermal model of section II-E. The efficiency map of the first scaled design Mot1 is reported in Fig. 18, highlighting the fulfillment of the torque versus speed requirements. Moreover, steady-state thermal analysis is run in Motor-CAD to validate the stall torque estimate and complete
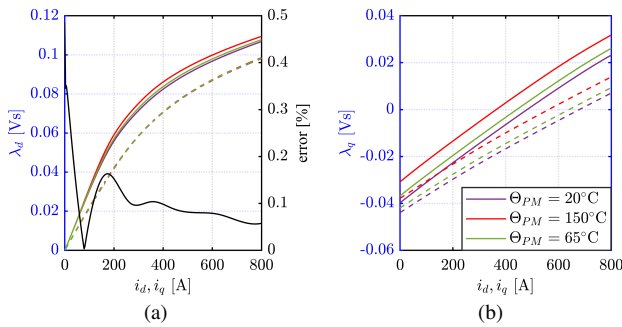
Fig. 15. Scaling plane for the design case 1. Target torque and speed contours are ticker lines. The domain of feasible machines is shaded in green. Chosen motor marked with a black dot.
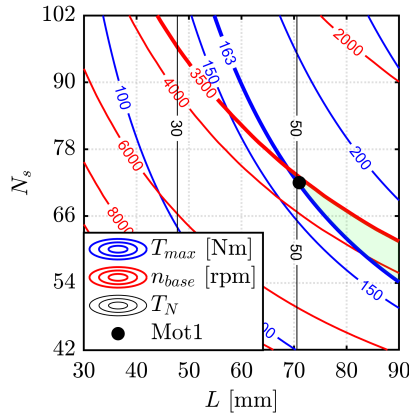


Fig. 17. Scaling plane of the design case 2. Target torque and speed contours are ticker lines. The domain of feasible machines is shaded in green. Chosen motors Mot2 and Mot3 marked with blue and green dots, respectively.

the continuous torque profile versus the operating speed. The process in Fig. 13 is employed to get the results displayed with a red line in Fig. 18. The results exhibit a valuable correspondence with the analytical estimation.

A dedicated stress analysis, displayed in Fig.16-a is run for Mot1, confirming the hypothesis of constant stress at maximum speed.

### B. Design case 2: same diameter and length of PRIUS IV

In this second example the diameter is set to the value of Prius IV MG2. The scaling ratio is imposed to:

$$k_D = \frac{D}{D_0} = \frac{215}{242} = 0.89 \qquad (24)$$

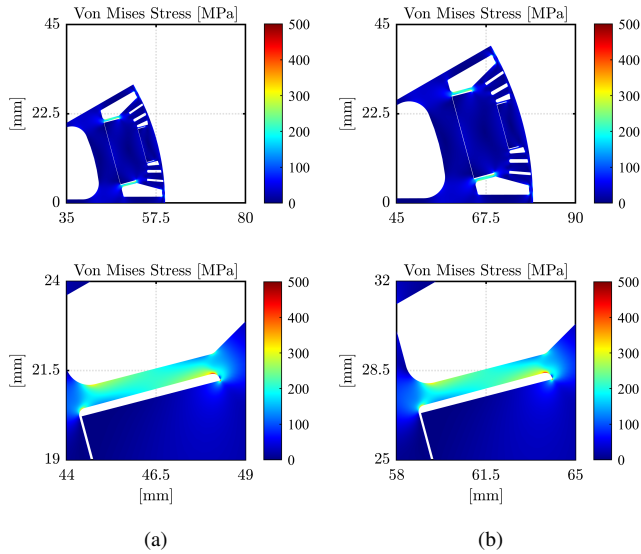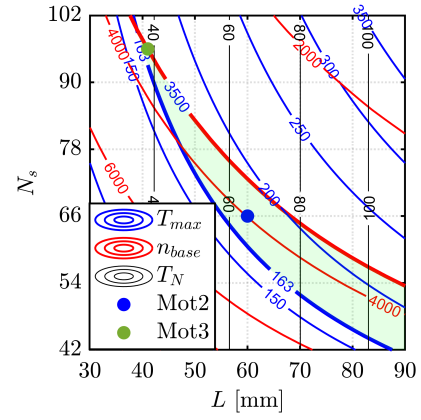and the expected maximum speed of the scaled machine is lower than the specified one (25).

$$n_{max} = \frac{n_{max0}}{k_D} = \frac{11400}{0.89} = 12800 \, rpm \qquad (25)$$

To match simultaneously the stack dimensions and the feasible maximum speed, a structural design adjustment would be needed. However, this goes beyond the scope of the paper which relates to scaling linearly all the dimensions of the stack cross section. The length-turns design plane of this second case is reported in Fig. 17 for $D = 176$mm and the same current and voltage limits of case 1. Taking as reference the stack length of the Prius MG2 and feasible number of turns, Mot2 is selected at $k_L = 0.45$ ($L = 60$mm) and $k_N = 3.66$ ($N_s = 60$). However, it is worth mentioning that the axial length could be reduced although maintaining the peak performance; this option is indicated as Mot3 in Fig. 17. Mot3 has a lower volume compared to Mot2 (and Prius). The stall torque is above 60 Nm for Mot2 and below 40 Nm for Mot3, which is expected from a shorter motor with the same peak performance. The efficiency map of Mot2 is reported in Fig. 18: also in this case the torque versus speed requirements are fulfilled. The thermal analysis confirms the predicted stall torque value. The stress analysis of Mot2 in Fig. 16-b confirms that the maximum stress condition is reached at 12800 rpm.



Fig. 16. Results of the mechanical FEA (a) for Mot1 at 17000 rpm and (b) for Mot2 at 12800 rpm.
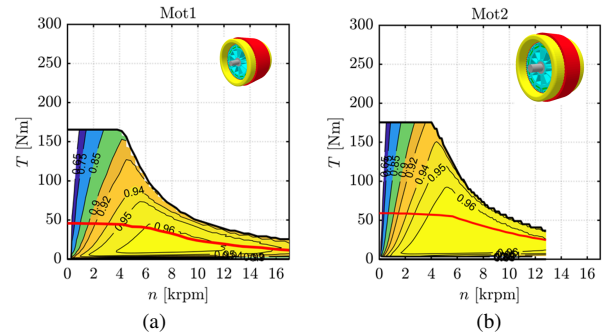


Fig. 18. Efficiency maps and continuous performance (red) of (a) the Mot1 and (b) of the Mot2.

TABLE III
PEAK PERFORMANCE AND DIMENSIONS OF THE MACHINES

|  |  | i3 | Mot1 | Mot2 |  |
|---|---|---|---|---|---|
| Peak torque | $T_{max}$ | 270 | 163 | 176 | [Nm] |
| Peak power | $P_{max}$ | 125 | 62 | 79 | [W] |
| Maximum speed | $n_{max}$ | 11400 | 17000 | 12800 | [rpm] |
| Nominal speed | $n_{base}$ | 4500 | 3580 | 3888 | [rpm] |
| Outer diameter | $D$ | 242 | 162 | 215 | [mm] |
| Stack length | $L$ | 132 | 71 | 60 | [mm] |
| Turns | $N_s$ | 18 | 72 | 66 |  |
| Active mass | $m_{act}$ | 31.3 | 10 | 15.8 | [kg] |
| Volume | $V$ | 6.1 | 1.5 | 2.2 | [L] |

TABLE IV
THERMAL DATA OF THE REFERENCE AND SCALED MACHINES

|  |  | i3 | Mot1 | Mot2 |  |
|---|---|---|---|---|---|
| Nominal torque | $T_N$ | 201 | 49 | 59 | [Nm] |
| Sustainable loss | $P_{cu}$ | 1951 | 994 | 1850 | [W] |
| Max Cu temperature | $\Theta_{Cu}$ | 180 | 180 | 180 | [°C] |
| Inlet temperature | $\Theta_{WJ}$ | 95 | 95 | 95 | [°C] |
| Fluid flow rate | $Q$ | 6 | 6 | 6 | [L/min] |
| Pump power | $P_{pump}$ | 1.61 | 1.73 | 1.19 | [W] |
| Channel height | $h_c$ | 4 | 2.68 | 3.55 | [mm] |
| Channel width | $w_c$ | 23 | 24.32 | 23.45 | [mm] |
| Axial spacer | $w_s$ | 8 | 8.46 | 8.16 | [mm] |
| Radial spacer | $h_s$ | 2 | 1.34 | 1.78 | [mm] |
| Pressure drop | $\Delta p$ | 0.16 | 0.17 | 0.12 | [bar] |
| Fluid velocity | $v$ | 1.09 | 1.53 | 1.20 | [m/s] |
| Conductivity | $h$ | 4391 | 6197 | 4848 | $[\frac{W}{°Cm^2}]$ |
| Surface conductivity | $h \cdot A$ | 548 | 313 | 548 | [W/°C] |

## V. CONCLUSION

A comprehensive scaling method is proposed for preliminary-design and system-level studies of traction PMSMs with liquid cooling jacket. Starting from a reference design, the stack diameter is scaled to fulfill the structural requirements dictated by the maximum operating speed of the final application. The new length-turns design plane is introduced, representing the peak torque and base speed contours of the scaled machine function of the stack length and number of turns. The design plane is based on scaled MTPA curves derived from the flux maps of the reference machine, and shows insightfully how the machine length can be minimized, provided that the corresponding number of turns is feasible. The guidelines for scaling the spiral water-glycol cooling jacket are provided and validated in simulation. The continuous torque at stall is well predicted by the proposed scaling laws and validated with Motor-CAD. Two e-motors are designed in seamless computational time with no extra FEA simulations, based on the specs of PRIUS IV MG2.

## VI. AKCNOWLEDGMENTS

## REFERENCES

[1] A. Krings and C. Monissen, "Review and Trends in Electric Traction Motors for Battery Electric and Hybrid Vehicles," in *2020 International Conference on Electrical Machines (ICEM)*, vol. 1, Aug. 2020.

[2] J. Benzaquen, J. He, and B. Mirafzal, "Toward more electric powertrains in aircraft: Technical challenges and advancements," *CES Transactions on Electrical Machines and Systems*, vol. 5, no. 3, Sep. 2021.

[3] V. Yaramasu, B. Wu, P. C. Sen, S. Kouro, and M. Narimani, "High-power wind energy conversion systems: State-of-the-art and emerging technologies," *Proceedings of the IEEE*, vol. 103, no. 5, May 2015.

[4] S. Nategh, A. Boglietti, Y. Liu, D. Barber, R. Brammer, D. Lindberg, and O. Aglen, "A Review on Different Aspects of Traction Motor Design for Railway Applications," *IEEE Transactions on Industry Applications*, vol. 56, no. 3, pp. 2148–2157, May 2020.

[5] Z. Wang, T. W. Ching, S. Huang, H. Wang, and T. Xu, "Challenges Faced by Electric Vehicle Motors and Their Solutions," *IEEE Access*, vol. 9, pp. 5228–5249, 2021.

[6] Z. Q. Zhu, W. Q. Chu, and Y. Guan, "Quantitative comparison of electromagnetic performance of electrical machines for HEVs/EVs," *CES Transactions on Electrical Machines and Systems*, vol. 1, 2017.

[7] R. Leuzzi, P. Cagnetta, F. Cupertino, S. Ferrari, and G. Pellegrino, "Performance assessment of ferrite- and neodymiumassisted synchronous reluctance machines," in *2017 IEEE Energy Conversion Congress and Exposition (ECCE)*, Oct. 2017, pp. 3958–3965.

[8] N. Rivière, M. Stokmaier, and J. Goss, "An Innovative Multi-Objective optimization Approach for the Multiphysics Design of Electrical Machines," in *2020 IEEE Transportation Electrification Conference & Expo (ITEC)*, Jun. 2020, pp. 691–696, iSSN: 2377-5483.

[9] R. Manko, M. Zagirnyak, M. Vukotic, M. Mavric, S. Corovic, M. Srekl, and D. Miljavec, "Design of experiment in optimization of permanent magnet synchronous motor performance," in *2017 International Conference on Modern Electrical and Energy Systems (MEES)*, Nov. 2017.

[10] S. Ferrari and G. Pellegrino, "FEAfix: FEA Refinement of Design Equations for Synchronous Reluctance Machines," *IEEE Transactions on Industry Applications*, vol. 56, no. 1, pp. 256–266, Jan. 2020.

[11] S. Stipetic, D. Zarko, and M. Popescu, "Ultra-fast axial and radial scaling of synchronous permanent magnet machines," *IET Electric Power Applications*, Aug. 2016.

[12] S. Stipetic, J. Goss, D. Zarko, and M. Popescu, "Calculation of Efficiency Maps Using a Scalable Saturated Model of Synchronous Permanent Magnet Machines," *IEEE Transactions on Industry Applications*, vol. 54, no. 5, pp. 4257–4267, Sep. 2018.

[13] F. Pauli, A. Ruf, and K. Hameyer, "Thermal Overload Capability of Permanent Magnet Synchronous Motors Employing Scaling Laws," in *XIII International Conference on Electrical Machines (ICEM)*, 2018.

[14] S. Chowdhury, E. Gurpinar, G.-J. Su, T. Raminosoa, T. A. Burress, and B. Ozpineci, "Enabling Technologies for Compact Integrated Electric Drives for Automotive Traction Applications," in *2019 IEEE Transportation Electrification Conference and Expo (ITEC)*, Jun. 2019.

[15] F. Cupertino and G. Pellegrino, "SyR-e: Synchronous Reluctance (machines) - evolution." [Online]. Available: www.github.com/SyR-e

[16] S. Ferrari, P. Ragazzo, G. Dilevrano, and G. Pellegrino, "Flux-Map Based FEA Evaluation of Synchronous Machine Efficiency Maps," in *2021 IEEE Workshop on Electrical Machines Design, Control and Diagnosis (WEMDCD)*, Apr. 2021, pp. 76–81.

[17] F. P. Incropera, Ed., *Fundamentals of heat and mass transfer*, 6th ed. Hoboken, NJ: John Wiley, 2007, oCLC: ocm62532755.

[18] P. Ragazzo, S. Ferrari, N. Riviere, M. Popescu, and G. Pellegrino, "Efficient Multiphysics Design Workflow of Synchronous Reluctance Motors," in *2020 International Conference on Electrical Machines (ICEM)*. Gothenburg, Sweden: IEEE, Aug. 2020, pp. 2507–2513.